

MI-BMInet: An Efficient Convolutional Neural Network for Motor Imagery Brain–Machine Interfaces with EEG Channel Selection

Xiaying Wang, *Student Member, IEEE*, Michael Hersche, *Student Member, IEEE*, Michele Magno, *Senior Member, IEEE*, Luca Benini, *Fellow, IEEE*

Abstract—A brain–machine interface (BMI) based on motor imagery (MI) enables the control of devices using brain signals while the subject imagines performing a movement. It plays a vital role in prosthesis control and motor rehabilitation. To improve user comfort, preserve data privacy, and reduce the system’s latency, a new trend in wearable BMIs is to execute algorithms on low-power microcontroller units (MCUs) embedded on edge devices to process the electroencephalographic (EEG) data in real-time close to the sensors. However, most of the classification models present in the literature are too resource-demanding, making them unfit for low-power MCUs. This paper proposes an efficient convolutional neural network (CNN) for EEG-based MI classification that achieves comparable accuracy while being orders of magnitude less resource-demanding and significantly more energy-efficient than state-of-the-art (SoA) models for a long-lifetime battery operation. To further reduce the model complexity, we propose an automatic channel selection method based on spatial filters and quantize both weights and activations to 8-bit precision with negligible accuracy loss. Finally, we implement and evaluate the proposed models on leading-edge parallel ultra-low-power (PULP) MCUs. The final 2-class solution consumes as little as 30 μ J/inference with a runtime of 2.95 ms/inference and an accuracy of 82.51% while using 6.4 \times fewer EEG channels, becoming the new SoA for embedded MI-BMI and defining a new Pareto frontier in the three-way trade-off among accuracy, resource cost, and power usage.

Index Terms—brain-machine interfaces, internet of minds, convolutional neural networks, feature extraction, embedded systems, edge computing, machine learning, tinyML

I. INTRODUCTION

A brain–machine interface (BMI) aims to translate brain activities into actionable information to control external devices, such as a wheelchair [1] or a prosthesis [2]. Besides clinical relevance for patients to regain lost abilities [3], recent developments in wearable technologies have pushed the field of BMI towards everyday life tasks in consumer products [4], [5], for example, to control robots [6] or drones [7], yielding improved user experience also for healthy subjects [8]. Motor

imagery (MI) is of great interest among the current BMI paradigms because it does not strictly depend on external stimuli; hence, it can be independently and asynchronously self-paced [9]. The MI-BMI decodes the user’s intention by analyzing the brain activities while the subject thinks of a movement of a body part without actually performing it [10].

A recent work by Zhuang et al. [11] has demonstrated the successful usage of MI-BMI in controlling ground vehicles using a wireless wearable device based on non-invasive electroencephalograms (EEGs). The data processing and the classification are executed on a remote engine, which leads to potential privacy concerns, a longer latency, and higher power consumption due to the data transmission. Recent achievements in low-power processing platforms and miniaturization enable the sensor data processing directly at the edge [12], [13]. By embedding algorithms at the sensor node, the data is analyzed locally, preserving privacy, reducing the energy consumption for a longer battery lifetime, and minimizing the system’s latency [14]. The decoded information can be directly sent to the controlled devices without any intermediate apparatus between the brain and the machines, empowering the future Internet of Minds (IoM) [15].

To achieve this goal, a smart wearable BMI has to satisfy a three-way trade-off among a) algorithmic performance: the embedded algorithm has to be able to complete the targeted task accurately; b) computational and storage parsimony: the complexity of the deployed algorithm has to meet the resource constraints of the edge platform in terms of memory footprint and runtime for a real-time application scenario; c) power: the power consumption must be low to guarantee a long-term continuous operation with long battery lifetime [14]. The low signal-to-noise ratio of the EEG data and the inter-session and inter-subject variability pose enormous challenges to obtaining high classification accuracy. Several machine learning (ML) and deep learning (DL) models have been proposed in the literature, achieving remarkable algorithmic performance [16], [17], [18]. However, the majority of them target only accuracy as a key metric while ignoring the resources required by the model, making them unfit for low-power microcontroller units (MCUs). For example, the Mr. Wolf processor [19] from the parallel ultra-low power (PULP) platform, a leading-edge example of high-performance and low-power MCU, has less than 600 kB of on-chip fast memory and can deliver up to 16.4 Giga operations per second (GOPS) of computational capability. It has been embedded in a wearable BMI device, called Biowolf,

Manuscript received November 07, 2019; revised January 16, 2020; accepted February 10, 2020.

X. Wang, M. Hersche, and L. Benini are with the Integrated Systems Laboratory, ETH Zürich, Switzerland (e-mail: xiaywang@iis.ee.ethz.ch). M. Magno is with the Center for Project-Based Learning D-ITET, ETH Zürich, Switzerland. M. Hersche is also with Cloud and AI Systems Research, IBM Research, Zürich, Switzerland. L. Benini is also with the Department of Electrical, Electronic and Information Engineering, University of Bologna, Italy.

This project was supported by the Swiss Data Science Center PhD Fellowship under grant ID P18-04.

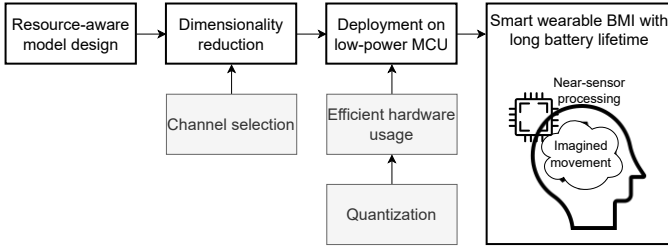


Fig. 1: Overview of the proposed methods for a smart wearable MI-BMI with embedded near-sensor processing.

with the minimal form factor of $40\text{ mm} \times 20\text{ mm} \times 2\text{ mm}$ and consuming less than 10 mW [12]. When considering very low-power MCUs in the sub-100-milliwatt power range, almost all the state-of-the-art (SoA) networks cannot be deployed on-board without additional expensive off-chip memory, yielding increased power consumption and longer execution latency. In full-precision representation, even the most compact EEG-Net [20] is out-of-reach by requiring more than 1 MB for storing the two biggest consecutive feature maps with the standard layer-by-layer execution during inference, making the deployment more challenging [21], [13]. In contrast, edge devices with more resources are too power-hungry and do not meet the specifications for long-term usage. Therefore, resource-friendly models that at the same time maintain high accuracy are desirable.

Besides considering the resource usage already during the model design, additional methods to reduce the model complexity are essential. In EEG applications, an important topic is the channel selection, where the EEG channels with more relevant features are selected for the final classification stage [22], [23]. In this work, we emphasize the importance of this technique not only for selecting the most significant features to improve accuracy but also for its advantages of reducing memory usage and computational complexity. Moreover, the reduction of EEG channels lowers the system’s power consumption since fewer analog front-end circuits are necessary for data acquisition, and it is fundamental for improving user comfort and achieving optimal device wearability. Another effective method to reduce the resource requirements is quantization, e.g., using 8 bits to represent numbers instead of 32 bits [24], [25]. It yields a significant reduction in memory usage and allows the use of efficient hardware units. Worth to be noted that both channel reduction and quantization pose challenges to the classification task and can lead to accuracy degradation due to the reduced number of inputs and numerical precision [21]. Hence, sophisticated algorithms are demanded to guarantee comparable accuracy while using minimal resources.

In this paper, we propose an end-to-end workflow for the realization of an energy-efficient wearable MI-BMI enabled with smart near-sensor computing, as shown in Fig. 1. We select MCUs based on PULP platforms [19], [26], because they have been demonstrated to outperform other families of low-power MCUs thanks to the parallel cores and the custom hardware extensions for digital signal processing (DSP) [27],

[28], [13], [29]. Our main contributions are as follows:

- We co-design a compact yet accurate convolutional neural network (CNN) for MI-BMI classification constrained to minimal hardware resources. It meets the tight resource limitations of ultra-low-power MCUs while being as accurate as the resource-demanding SoA algorithms. We evaluate the performance in both inter-session and inter-subject challenges using two publicly available MI datasets, namely the BCI Competition IV-2a and the Physionet EEG Motor Movement/Imagery (MM/MI), and achieve respectively 76.03% , 65.62% accuracy on the 4-class task and 86.32% , 82.79% on the 2-class task.
- We reduce the input dimensions by automatically selecting the most relevant EEG channels to limit further the model complexity and the memory footprint while maintaining similar classification accuracy (82.79% vs. 82.51% for the 2-class task of the MM/MI dataset) or even improving the accuracy by up to 1.33% in the case of the subject-specific models of the IV-2a dataset.
- We quantize both model weights and activations to 8-bit precision with negligible effect on the classification accuracy to further reduce the memory usage and optimally exploit the hardware extensions. We efficiently deploy the quantized models on ultra-low-power MCUs, achieving an energy consumption of merely $30\text{ }\mu\text{J}$ per inference and real-time execution of 2.95 ms . With a $6.4\times$ reduction of EEG channels, the battery operation time can be increased from 3.8 up to 22 hours.

This work successfully satisfies the three-way trade-off among performance, cost, and power [14] by maximizing the algorithmic accuracy, minimizing the computational cost, and minimizing the power consumption for a real-time smart wearable MI-BMI with an extended battery lifetime, paving the way to the future IoM¹.

II. RELATED WORKS

We discuss the related works based on the popular BCI Competition IV-2a dataset [30], [31] and the Physionet EEG MM/MI dataset [32], [33]. The former is the most representative for subject-specific models and inter-session challenges, whereas the latter includes a remarkable number of subjects and is often used to tackle the inter-subject variability. We select only the works that follow the competition rules for the IV-2a dataset or train a global model validated on unseen subjects for the MM/MI dataset for a correct and fair comparison. As this paper covers the full flow of model design, channel selection, and embedded implementation, we divide the discussion of the related works accordingly.

A. Classification Models

Traditional ML-based approaches require manual feature extraction, based on which a classifier is trained to solve the task. The most common and effective methods to extract discriminative features in MI-BMIs are based on the Common Spatial Patterns (CSP) [34], [35] and the Riemannian

¹We will release open-source code after review.

geometry [36]. The authors in [22] and [37] propose spatial or temporal filtering based on CSP, reaching a 2-class classification accuracy of 80.56% and 79.6% on the IV-2a dataset, respectively. The work in [38] compares the CSP and Riemannian methods and demonstrates that Multiscale Riemannian Classifier (MRC) achieves the best 4-class classification accuracy of 75.47% using multiple time windows with a support vector machine (SVM). A more recent work [29] based on MRC reduces the number of features and achieves a 4-class accuracy of 76.4% using different classifiers for each subject. By combining Filter-Bank Common Spatial Patterns (FBCSP), autoregressive models, and feature selection with mutual information, the work in [39] achieves the highest 2-class accuracy of 86.01%. The authors generalize the methods to the 4-class task obtaining a Cohen's kappa coefficient of 0.61. Similar techniques of feature extraction are used in [40] with Adaptive Boosting classifier, resulting in an improved kappa value of 0.646.

In another vein, DL methods enable the classification of BMI tasks without handcrafted features. Many works have demonstrated the effectiveness of CNNs in learning temporal and spatial features obtaining accuracy values ranging from 79.9% up to 86.96% for 2-class tasks [16], [18] and 74.31% to 77.35% for 4-class tasks [17], [41], [42], [13], [43]. With additional hyperparameters tuning specific to each subject, the accuracy can be improved up to 83.84% on the 4-class task [42]. For the inter-subject cases on MM/MI dataset, the 2- and 4-class accuracy values range from 80.38% to 83.26% and 58.58% and 65.07%, respectively [44], [21], [23]. One major drawback of the DL approach is that the models tend to grow in size, increasing the demand for computational and storage resources. FB3DCNN achieves the SoA accuracy (86.96%) in the 2-class task of the IV-2a dataset, but it requires storage for 46 million parameters [18], [42]. EEG-TCNet and EEG-ITNet perform best in the 4-class task (77.35% and 76.74%, respectively) and have significantly fewer parameters (below 5 k) [42], [43]. However, when considering the standard layer-by-layer computation schedule, the additional memory footprint required during the execution time is up to two orders of magnitude more than the number of parameters, making them significantly more challenging for very low-power MCUs. In this paper, we propose a more compact CNN with less than 50 k parameters *and features* to be stored during the inference time. The resource requirement is orders of magnitude lower than recent related works [17], [41], [42], [18] while achieving similar classification accuracy.

B. Channel Selection

It is beneficial to reduce the number of EEG channels for improved user comfort, a reduced setup time, a lower power consumption, and a decreased model complexity. The authors in [22] have proven that input EEG channels can be effectively reduced subject-specifically from 22 to an average of 8.11 while improving the 2-class accuracy on the IV-2a dataset by around 3% using CSP-based methods. A more recent work [45] uses a fixed number of 15 channels for all subjects reaching an accuracy of 79.19%. It is 4.42% less than [22],

demonstrating that selecting a variable number of channels for each subject is beneficial. The authors in [46] combine CSP with Riemannian distances obtaining an SoA classification accuracy of 77.82% and a kappa value of 0.71 with an average of 15.2 selected channels over the nine subjects of the IV-2a dataset for the 4-class MI task. CNN-based channel reduction approaches are also found in the literature [44], [23]. Dose et al. [44] manually select subsets of EEG channels to compare with related works and demonstrate that their proposed architecture based on the shallow ConvNet [16] outperforms most other models. More recent work by Tokovarov et al. [23] applies an automatic channel selection method based on CNN feature maps obtaining 82.34% accuracy with only 14 instead of 64 channels on the 2-class MI task of the MM/MI dataset outperforming the manual selection of [44]. Given the many advantages of channel selection, in this work, we propose an automatic method based on the spatial filters of the proposed CNN. It can effectively reduce the number of channels from 64 to 10 for the MM/MI dataset, with the advantage of $1.3\times$ fewer parameters, $3.1\times$ less memory footprint, and $1.4\times$ lower computational complexity while having a negligible accuracy drop of 0.28% for the 2-class inter-subject task. The inter-session accuracy of the subject-specific models for the IV-2a dataset is increased by up to 1.33%, with an average channel reduction of 60% for the 2-class task.

C. Embedded Implementation

Over the recent years, increasing attention has been gained by the embedded deployment of ML and DL models on low-power edge devices, nourishing the fast-growing field of TinyML [47] and giving birth to notable projects such as TensorFlow Lite [48]. Some initial efforts can be also found in the BMI literature. Belwafi et al. [49] propose a CSP-based approach implemented in 16-bit precision on a Stratix-IV field-programmable gate array (FPGA) board with a power consumption of 700 mW. It achieves a 2-class accuracy of 78.85% on the IV-2a dataset with an inference time of 430 ms and energy consumption of 301,000 μ J. Another embedded implementation based on CSP can be found in [50]. The accuracy on the IV-2a dataset is 80.55% and 67.21% for 2- and 4-class tasks, respectively. The methods are implemented in 20-bit precision on a Virtex-6 FPGA consuming 83.90 mW and taking up to 11.66 ms (i.e., 978 μ J).

Two other works have implemented DL-based approaches for MI-BMI on embedded devices [21], [13]. The authors in [21] deploy an EEGNet-based CNN on two STMicroelectronics MCUs featuring ARM Cortex-M4 and M7. The model requires too much memory for the selected low-power MCUs based on the X-CUBE-AI deployment tool provided by the manufacturer. Hence, the input signals are downsampled, shortened in time, and 38 manually selected EEG channels are used. The 4-class accuracy on the MM/MI dataset drops by 2.56% on the Cortex-M4 due to the limited hardware resources. The embedded model with the highest accuracy (64.76%) could be implemented only on the Cortex-M7, which provides more resources but consumes one order of magnitude more power than the Cortex-M4. The model with the

highest accuracy takes 43.81 ms and consumes 18,100 μJ per inference. A more energy-efficient implementation is proposed in [13], outperforming all previous solutions based on FPGAs and Cortex-M MCUs. The model is first quantized to 8-bit fixed-point representation with negligible loss in accuracy and implemented on Mr. Wolf, consuming only 11.75 mW. The average quantized accuracy over the nine subjects of the IV-2a dataset is 70.9% for the 4-class MI task. The energy consumption is 337 μJ , and the inference time is 28.67 ms. However, the classification accuracy is relatively low, and the proposed solution is not flexible because it is designed specifically for EEGNet and it abandons the common layer-by-layer paradigm adopted by most deployment frameworks [47].

A very recent work [29] proposes an MRC implementation with a combination of 8-, 16-, and 32-bit fixed-point and 32-bit floating-point representations on the new PULP MCU called Vega [26]. It is currently the SoA in terms of accuracy and energy efficiency (74.1% 4-class quantized accuracy, 16.9 ms inference time, and 198 μJ energy consumption).

In this work, we quantize the proposed CNN to 8 bits achieving a 4-class quantized accuracy of 75.63%. The full-channel implementations for the IV-2a dataset take 11.37 ms and 5.10 ms and consume 114 μJ and 60.5 μJ on Mr. Wolf and Vega, respectively. It is 4.7% and 1.5% more accurate than [13] and the SoA [29]. The inference execution is $2.5\times$ and $3.3\times$ faster, and it consumes $3\times$ and $3.3\times$ less on the same MCUs, respectively. The energy consumption is further lowered by reducing the number of EEG channels without significantly affecting the accuracy.

III. METHODS

The workflow proposed in this paper is as follows: first, an accurate classification model is designed by taking into consideration hardware constraints; second, EEG channel selection is performed to reduce the input dimensionality yielding more energy-efficient models; third, the model is quantized to minimize further the resource usage and is efficiently deployed on the selected MCUs by exploiting the hardware extensions.

A. Network Architecture and Resource Requirements

As motivated in the introduction, our target is low-power MI-BMIs, meaning that the classification model has to respect strict resource availability. Hence, while designing the network, we also assess the memory footprint and the computational complexity. Additionally, unlike most previous works, which consider only the number of parameters, we propose a more accurate estimation of the memory usage based on the standard layer-by-layer computation schedule. This is especially crucial for embedded deployment [51].

Fig. 2 depicts the proposed model named MI-BMInet. The input array is arranged such that each row represents the EEG signals from the electrodes, and each column is the sample at every time point. The dimension is $N_{ch} \times N_s$, with N_{ch} being the number of EEG channels and N_s the number of samples. Many works in literature have demonstrated that temporal and spatial features most successfully decode the EEG signals, as they represent the temporal and spatial summation of

brain activities [16], [20], [41], [42], [43]. In all previous works, the extraction of the temporal information causes a significant increase in memory usage and computations, leading to deployment difficulties [21], [13]. In our proposed CNN, we also extract temporal and spatial features, as this is currently the most effective approach for EEG signals, but, in contrast to previous works, we reduce the dimensionality by first extracting the spatial features, followed by the extraction of the temporal information. This way, the memory and the computation overhead are effectively reduced.

More precisely, the input is passed to a first depthwise convolutional layer with N_k one-dimensional kernels of size $N_{ch} \times 1$ to find spatial correlations among the EEG channels, followed by a batch normalization layer. This spatial convolution outputs N_k feature maps of dimension $1 \times N_s$. These are subsequently filtered using another layer of depthwise convolution with N_k kernels of dimension $1 \times N_f$ applied along the temporal dimension to learn temporal information. The number of parameters in a depthwise convolutional layer can be calculated as $N_k \cdot (k_H \cdot k_W)$, with k_H and k_W being the height and width of the kernels, reported in brackets in Fig. 2. Additionally, each batch normalization layer has $4 \cdot f$ parameters, with f being the number of feature maps, which corresponds to the number of filters N_k in the case of depthwise convolutions. Afterward, a separable convolution, i.e., a depthwise convolution followed by a pointwise convolution, is applied to extract additional spatio-temporal features using N_k filters of size 1×16 . This amounts to $N_k \cdot (1 \cdot 16) + N_k \cdot N_k$ parameters. Rectified Linear Unit (ReLU) is chosen as activation since it is the most hardware-friendly non-linear activation function. Additionally, average pooling layers with a kernel size of 8×1 are applied in the time domain to reduce the dimensions of the feature maps. Finally, a fully connected layer computes the classification output. It presents $(N_{in} + 1) \cdot N_{out}$ parameters, with N_{in} being the number of input nodes and N_{out} the output nodes, i.e., N_{cl} .

Besides the network weights, the input and the output feature maps need to be stored during the computation of a layer. As an example, the size of the input and the output feature maps of the first convolutional layer is $N_{ch} \cdot N_s + N_k \cdot N_s$, which has to be stored contemporaneously in the memory during the computation time. Note that this memory can be reused for the next layer once the computation of the previous one is completed. Hence, the biggest sum of two consecutive feature maps dictates the required memory footprint.

We further estimate the complexity of the model as the sum of the number of multiply-and-accumulate (MACC) operations in the convolutional and fully connected layers. The number of operations in each depthwise convolutional layer is $(k_H \cdot k_W) \cdot (H_{out} \cdot W_{out}) \cdot N_k$, with H_{out} and W_{out} being respectively the height and the width of the output feature maps. While for the separable convolution, we estimate $(H_{out} \cdot W_{out}) \cdot ((1 \cdot 16) + N_k)$ MACC operations. Finally, the fully connected layer requires $N_{in} \cdot N_{out}$ operations.

B. EEG Channel Selection

We propose an automatic channel selection method based on the spatial filters of MI-BMInet to reduce further the resource

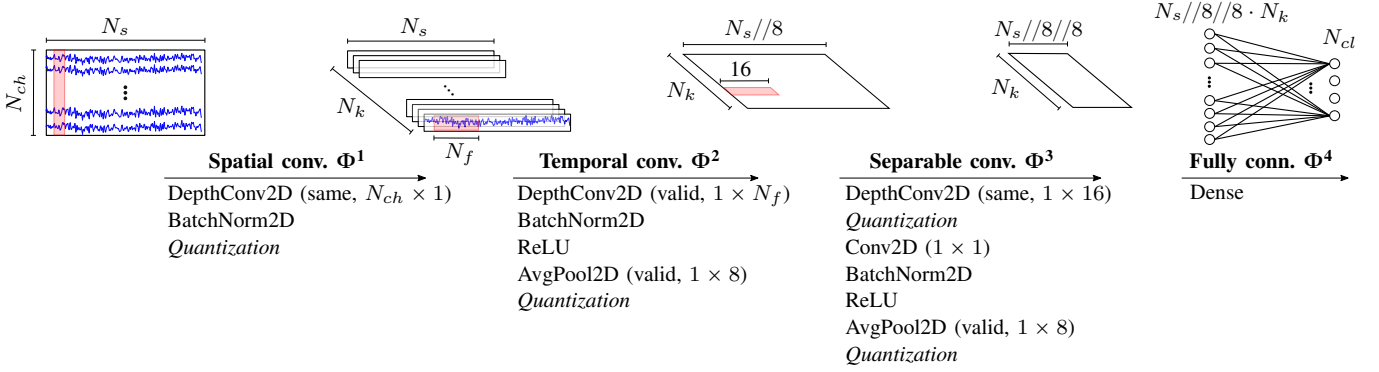


Fig. 2: Architecture of MI-BMInet. N_s is the number of input samples in the time domain, N_{ch} the number of EEG channels, N_{cl} the number of classes, N_f the filter size of the temporal filter, and N_k is the number of filters. The padding strategy and the kernel size are reported in brackets. The addition of the quantization layers is highlighted in *italic*.

requirements. Given a pretrained model on all N_{ch} EEG channels and W_S , the weights of the first spatial convolutional layer with dimension $N_{ch} \times N_k$, we compute the ℓ_2 -norm for each EEG channel $i_{ch} = 1, 2, \dots, N_{ch}$ as

$$\|w_S\|_2(i_{ch}) = \sqrt{\sum_{n=1}^{N_k} |w_S(i_{ch}, n)|^2}, \quad (1)$$

which gives the vector's magnitude of the weights corresponding to each EEG channel. We subsequently select \bar{N}_{ch} channels with the biggest $\|w_S\|_2$ amplitudes, with \bar{N}_{ch} being the desired number of EEG electrodes. Algorithm 1 shows the pseudo-code of the proposed method.

For comparison, we implement two additional manual channel selection methods: one based on the whole scalp as in [21]; the other one targets the specific brain region of the sensorimotor cortex such that the EEG electrodes can be embedded into smart wearable headphones, e.g., Versus headset [52] or Melomind [53], for better user acceptance. Fig. 1 in the Appendix shows the positions of the 64 electrodes for the MM/MI dataset and the 22 channels filled with yellow used in the IV-2a dataset. We select three configurations that are evenly distributed over the entire scalp to directly compare with [21] on the MM/MI dataset: a) 19 electrodes

based on the international 10-20 system (excluding A1 and A2), encircled with green dashed lines; b) 38 electrodes by adding intermediate positions, encircled with solid blue lines; c) 8 electrodes based on Bitbrain headset, encircled with dash-dotted red lines. The distributed configurations are not evaluated on the IV-2a dataset because of the reduced number of available electrodes.

Furthermore, we manually select the EEG channels covering the sensorimotor cortex, where most of the brain's activations during motor movement (MM) and MI are identified, especially around C3 and C4 [10]. This region is also physically covered by the users' audio headphones that are commonly accepted and worn nowadays for extended time periods. This means we can embed the EEG electrodes on a wearable device already widely used in daily life. This setup is much less obtrusive and aesthetically more acceptable than traditional EEG caps. Hence, we select subsets of electrodes from the central line covering the C3 and C4 electrodes, as highlighted in Fig. 1 in the Appendix with the red-shaded background. In addition, we separately and incrementally include subsets of adjacent electrodes towards the front and the back of the head, respectively shaded with the green and blue background color. Table I in the Appendix reports all the configurations with the selected subsets of channels over the sensorimotor cortex for the MM/MI dataset. The same is done for the IV-2a dataset with the available electrodes.

Additional comparisons with CSP- and Riemannian-based methods are discussed in Sec. IV.

Algorithm 1: Pseudo-code for automatic EEG channel selection based on spatial filters of the proposed CNN.

Data: Pretrained model on all N_{ch} channels.

Result: Indexes of \bar{N}_{ch} selected channels.

begin

Load the pretrained model;
 Extract W_S , the weights of the spatial convolution;
for each EEG channel i_{ch} **from** 0 **to** $N_{ch} - 1$ **do**
 Calculate the ℓ_2 norm

$$\|w_S\|_2(i_{ch}) = \sqrt{\sum_{n=1}^{N_k} |w_S(i_{ch}, n)|^2}$$

Find the indices that sort $\|w_S\|_2(i_{ch})$ in descending order;
 Take the first \bar{N}_{ch} indices;

C. Embedded Implementation

To optimally deploy MI-BMInet on low-power MCUs, we first quantize the models to 8-bit representations using quantization-aware training to reduce further the memory footprint and to exploit the hardware extensions. Subsequently, we deploy the quantized networks on the selected MCUs and measure the inference runtime and the power consumption.

1) *Quantization:* We quantize both weights and activations of MI-BMInet, including the input signals, from 32-bit floating-point to 8-bit fixed-point values. To preserve the classification accuracy, we perform quantization-aware training.

The addition of the quantization layers is shown in Fig. 2. The quantization procedure is as follows:

- The network is trained in full precision until epoch t_a ;
- At epoch t_a , the quantization of the activations starts using the straight-through estimator (STE) [54]. The network is readjusted on the quantized activations until epoch t_w ;
- From epoch t_w until epoch t_{end} , the weights are increasingly quantized using Random Partition Relaxation (RPR) [25] at a step size of 10.

2) *Network Deployment*: We implement the 8-bit quantized networks on RISC-V-based PULP Mr. Wolf [19] and Vega [26]. The former has been embedded into Biowolf, the SoA BMI system in terms of power consumption, computational capability, and form factor [12]. While the latter is a more recent microprocessor with improved design and technology, presenting the SoA energy efficiency. They both feature a System-on-Chip (SoC) domain with a single core for handling peripherals and simple computations and a cluster domain with eight and nine parallel cores for more compute-intensive tasks. The cluster cores are based on RV32IMCF Instruction Set Architecture (ISA) with additional custom extensions for DSP applications, including hardware loops, post-incremental load and store instructions, and support for two-way and four-way Single Instruction, Multiple Data (SIMD) operations.

We propose a manual implementation of the quantized models, as currently, no deployment tools directly support the selected MCUs. However, we follow the same layer-by-layer schedule to better demonstrate the deployment feasibility of our models. We take inspiration from [13] and merge the conversion factor of the quantization with the bias and the scaling factor of the batch normalization layers and reorder the batch normalization, the ReLU, and the pooling layers to reduce the number of divisions since they are expensive operations requiring many computational cycles and introduce rounding errors. Moreover, we implement a concurrent computation of the feature maps using the parallel cores and exploit the four-way SIMD for executing four MACC operations on the 8-bit quantized numbers in a single cycle. We export the network weights in the reversed order with respect to convolutions to use the optimized 1-D cross-correlation functions from the PULP-DSP library [55]. We implement the data handling and the computation of each layer such that the data locality is preserved and the custom ISA extensions are effectively used.

IV. EXPERIMENTS AND RESULTS

We use Keras with TensorFlow v1.11 backend to train full-precision models. We apply our methods to two SoA datasets to tackle both inter-session and inter-subject variability.

a) *BCI Competition IV-2a* [30], [31]: Four MI tasks are recorded from 9 subjects using 22 EEG channels, namely the imagined movements of the left hand (L), right hand (R), both feet (F), and tongue (T). The data is collected on two days (i.e., sessions) at 250 Hz sampling frequency and provided after a bandpass filter between 0.5 Hz and 100 Hz. Each recording session contains 288 trials, of which 9.41%

are marked by an expert as artifacts and are removed. We perform 2-, 3-, and 4-class classification using L/R, L/R/F, and L/R/F/T MI tasks, respectively, and consider a time window of 3 s starting from the appearance of the MI cue. We conduct subject-specific validation using the EEG data of the first session for training and the second for testing, as stated in the competition rules. The models are trained with the Adam optimizer for 500 epochs with a batch size of 32, a fixed learning rate of 0.001, and 1e-7 as the default epsilon value for numerical stability. The cross-entropy loss is used. We repeat the experiments 25 times and report the average results to consider the training variability. We calculate both classification accuracy and Cohen’s kappa score as it is often done with this dataset.

b) *Physionet EEG MM/MI* [32], [33]: The data is recorded at 160 Hz using 64 electrodes. 105 subjects are effectively considered from this dataset. Every subject performed a total of six MI runs: three runs of the left fist (L) against the right fist (R) and three runs of both fists (B) against both feet (F). We additionally extract windows of 3 s from the baseline runs with eyes open to obtain trials with resting EEG data (0). In total, we have 21 trials per class per subject. As in [44], we perform 2-, 3-, and 4-class MI classification using L/R, L/R/0, and L/R/0/F MI tasks, respectively, and consider a time window of 3 s starting from the appearance of the cue. We use 5-fold cross-validation (CV) across the subjects, i.e., the model is trained on the data from a subset of subjects and is validated on the data from the remaining unseen subjects. The models are trained with Adam optimizer for 100 epochs with a batch size of 16. A fixed learning rate scheduler reaches the best performance; more precisely, the learning rate is set to 0.01, 0.001, and 0.0001 at epochs 0, 40, and 80, respectively. Cross-entropy loss is used. Similar to the IV-2a dataset, we repeat the 5-fold CV procedure five times and obtain an average accuracy over 25 experiments to account for the training variability.

A. Network Architecture

Based on the performance achieved with hyperparameters tuning, we choose the filter size N_f to be 64 and 128 and the number of filters N_k to be 32 and 16 for the IV-2a and the MM/MI dataset, respectively. As reported in Table I, our model requires around 6.1 k and 4.2 k parameters in full-channel configuration. The two biggest consecutive feature maps contain 40.5 k and 38.4 k feature values for the IV-2a

TABLE I: Resource estimation considering all EEG channels and the 4-class task. The two biggest consecutive feature maps are marked in *italic* and the total resource requirements in **bold**.

| Layer | BCI Comp. IV-2a <i>$N_{ch}=22, N_s=750, N_k=32, N_f=64$</i> | | | Physionet MM/MI <i>$N_{ch}=64, N_s=480, N_k=16, N_f=128$</i> | | |
|-------------|---|---------------|------------------|--|---------------|------------------|
| | #params | #features | #MACC | #params | #features | #MACC |
| Input | | <i>16,500</i> | | | <i>30,720</i> | |
| Φ^1 | 704+128 | <i>24,000</i> | 528,000 | 1,024+64 | <i>7,680</i> | 491,520 |
| Φ^2 | 2,048+128 | 3,000 | 1,536,000 | 2,048+64 | 960 | 983,040 |
| Φ^3 | 1,536+128 | 176 | 96,000 | 512+64 | 112 | 30,720 |
| Φ^4 | 1,412 | 4 | 704 | 484 | 4 | 448 |
| Tot. | 6,084 | 40,500 | 2,209,408 | 4,228 | 38,400 | 1,505,728 |

TABLE II: Comparison of accuracy and kappa values (κ) in full-channel, full-precision configuration. The publication year follows the apostrophe. The total number of parameters, the maximum number of consecutive features, and the number of MACC operations are estimated on the 4-class task when available, otherwise on the 2-class task. The proposed solution is highlighted in bold.

| | Accuracy [%]/ κ | | Tot. # params | Max. # cons. f. | Tot. # MACC |
|----------------------------------|------------------------|-------------------|------------------|--------------------|----------------|
| | 2- | 4-class | | | |
| BCI Comp. IV-2a | | | | | |
| CSP'15 [22] | 80.56/- | -/- | - | - | - |
| MRC'18 [38] | -/- | 75.47/- | - | - | - |
| FBCSP'20 [40] | -/- | -/0.65 | - | - | - |
| JSTFD+LDA'20 [37] | 79.6/- | -/- | - | - | - |
| MI-TS'20 [39] | 86.01/- | -/0.61 | - | - | - |
| MRC'21 [56], [29] [†] | -/- | 75.10/- | - | - | - |
| S. ConvNet'17 [16] | 79.90/- | 74.31/0.66 | 47.3 k | 1,013 k | 63.0 M |
| EEGNet'18 [20] | -/- | 71.30/- | 2.63 k | 223 k | 12.98 M |
| MSFBCNN'19 [17] | -/- | 75.80/- | 155 k | 5,775 k | 202 M |
| MCNN'19 [41] | -/- | 75.7/- | 14 M | 574 k | 103 M |
| EEG-TCNet'20 [42] [‡] | -/- | 77.35/0.70 | 4.27 k | 396 k | 6.8 M |
| FB3DCNN'21 [18] | 86.96/- | -/- | 46 M | 472.1 k | 62.3 M |
| EEG-ITNet'22 [43] | -/- | 76.74/- | 5.2 k | 74.3 k | 7.36 M |
| MI-BMInet* | 86.32/0.73 | 76.03/0.68 | 6.08 k | 40.5 k | 2.21 M |
| Physionet MM/MI | | | | | |
| S. ConvNet'18 [44] | 80.38/- | 58.58/- | 203 k | 1,260 k | 86.12 M |
| EEGNet'20 [21] [§] | 82.43/- | 65.07/- | 3.2 k | 277.56 k | 31.98 M |
| CNN'20 [23] | 83.26/- | -/- | 235 k | 122.88 k | 33.61 M |
| MI-BMInet* | 82.79/- | 65.62/- | 4.23 k | 38.40 k | 1.51 M |

[†] Improved to 76.4% using different classifiers for each subject.

[‡] Improved to 83.84%/0.78 using subject-specific hyperparameters.

^{||} Adapted and reproduced in [18], [42], [13]. [§] Based on [20].

* Respectively 80.37%/0.71 and 74.92% for 3-class task.

and the MM/MI datasets. This means that the execution of MI-BMInet requires the memory storage for only 46.6k and 42.6k values, comprehensive of both model parameters and the maximum number of features during inference. It is at least $1.7\times$ [43] and up to two orders of magnitude [17], [41], [18] less than the related works reported in Table II.

When comparing the computational complexity, MI-BMInet requires the least number of MACC operations, i.e., down to 2.21 million for the IV-2a dataset and 1.51 million for the MM/MI dataset. In contrast to the most compute-intensive related works [17], [44], our models require $91\times$ and $57\times$ fewer computations while being 0.23% and 7.04% more accurate on the IV-2a and MM/MI datasets, respectively. More recent works have reduced the computational complexity [42], [18], [43]; however, our model still requires at least $3\times$ fewer computations. This directly correlates with the computational latency during inference time, as shown in Sec. IV-C.

Despite the significantly fewer resource requirements, the accuracy of MI-BMInet is overall comparable to recent SoA models. More specifically, the accuracy values are 86.32%, 80.37%, 76.03% (IV-2a), and 82.79%, 74.92%, 65.62% (MM/MI), respectively for 2-, 3-, 4-class tasks. The highest 4-class accuracy on the IV-2a dataset following the competition rules is around 77% without additional subject-specific hyperparameters tunings [42]. The authors have improved the accuracy to about 84% with variable networks. As more details are needed to understand the reason behind this accuracy

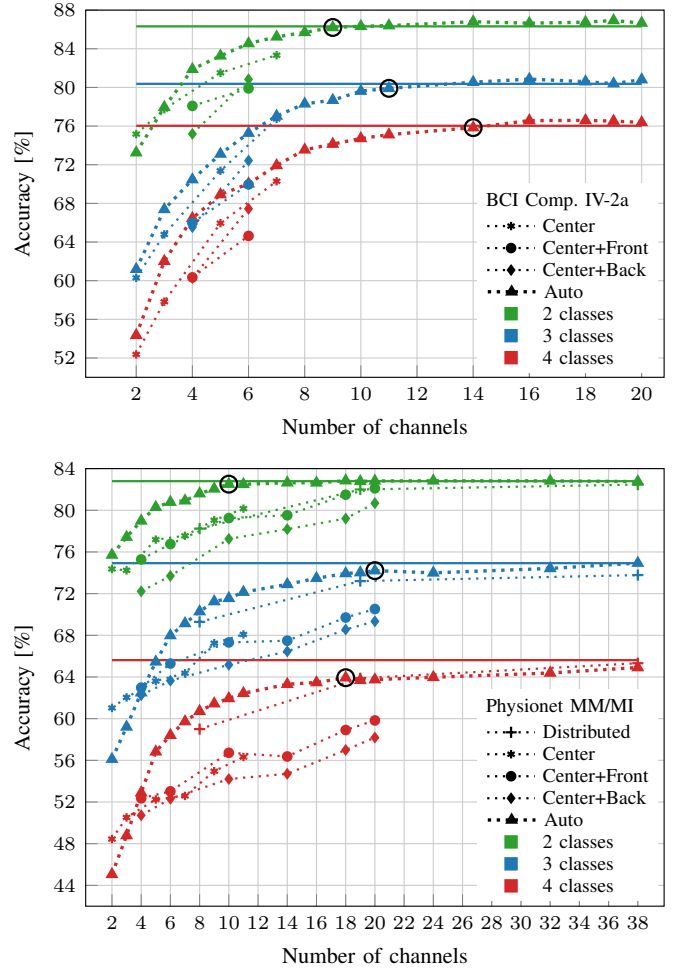


Fig. 3: Channel selection accuracy averaged over subjects for the IV-2a dataset (top) and over CV folds for the MM/MI dataset (bottom). The solid lines indicate the full-channel accuracy and the circles mark the optimal number of channels.

increase, we discuss this comparison separately in Sec. V. More recent works achieve 86.96% and 76.74% 2- and 4-class accuracy values (less than 0.71% difference from ours) but demand significantly more resources, i.e., $997.3\times$ and $1.7\times$ more parameters and features, and $28.2\times$ and $3.3\times$ more MACCs [18], [43].

B. EEG Channel Selection

As shown in Fig. 3, our automatic method consistently outperforms the manual selection methods. It can reduce, on average, the number of channels down to 9, 11, and 14 across the 9 subjects of the IV-2a dataset while retaining similar average accuracy (86.21%, 79.91%, 75.84%) as the baseline, represented with solid lines (86.32%, 80.37%, 76.03%), respectively for the 2-, 3-, and 4-class tasks. In some cases, slightly better accuracy is achieved compared to the full-channel baseline thanks to the subject-specific methodology. We report the best accuracy for each subject with the corresponding number of channels in Table III. The average accuracy is improved by up to 1.33%. The best performing

TABLE III: Classification accuracy (%) / kappa score with all channels and the best accuracy / kappa score for each subject with the corresponding number of selected channels (in brackets) on the IV-2a dataset and comparison with related works. The best accuracy values are highlighted in bold. The publication year is indicated with the apostrophe.

| S. | 2-class | | | | | 3-class | | 4-class | | |
|-------|-------------------|--------------------------|----------------|---------------------|---------------------|-------------------|--------------------------|-------------------|------------------------|--------------------------|
| | MI-BMInet | | CSP'15 [22] | | M-CSP'19 [45] | MI-BMInet | | MI-BMInet | | CSP+Riem.'20 [46] |
| | all ch. | sel. ch. | all ch. | sel. ch. | sel. ch. | all ch. | sel. ch. | all ch. | sel. ch. | sel. ch. |
| 1 | 84.03/0.68 | 86.98/0.74 (4) | 90.78/- | 83.36/- (9) | 90.78/- (15) | 89.43/0.84 | 91.18/0.87 (14) | 83.10/0.78 | 84.41/0.80 (20) | 87.51/0.81 (14) |
| 2 | 71.15/0.42 | 72.65/0.45 (20) | 59.85/- | 71.83/- (11) | 57.75/- (15) | 65.74/0.49 | 68.76/0.53 (16) | 59.27/0.46 | 60.49/0.47 (18) | 58.32/0.44 (18) |
| 3 | 94.95/0.90 | 94.95/0.90 (22) | 97.81/- | 98.54/- (13) | 97.08/- (15) | 91.67/0.88 | 92.18/0.88 (18) | 90.64/0.88 | 90.97/0.88 (18) | 89.01/0.86 (14) |
| 4 | 74.38/0.49 | 76.66/0.53 (9) | 68.10/- | 74.13/- (3) | 70.69/- (15) | 75.66/0.64 | 76.00/0.64 (14) | 69.77/0.60 | 70.63/0.61 (18) | 71.12/0.63 (15) |
| 5 | 92.00/0.84 | 93.84/0.88 (4) | 68.88/- | 71.11/- (4) | 61.48/- (15) | 79.17/0.70 | 80.33/0.71 (18) | 71.83/0.62 | 73.61/0.65 (19) | 63.44/0.49 (19) |
| 6 | 79.48/0.59 | 81.11/0.62 (20) | 66.67/- | 73.14/- (8) | 70.37/- (15) | 63.48/0.45 | 65.56/0.49 (20) | 58.10/0.44 | 59.91/0.47 (11) | 60.16/0.53 (11) |
| 7 | 90.51/0.81 | 91.17/0.82 (20) | 82.14/- | 83.57/- (6) | 72.14/- (15) | 88.49/0.83 | 88.97/0.84 (18) | 84.71/0.80 | 85.76/0.81 (19) | 93.14/0.92 (15) |
| 8 | 98.06/0.96 | 98.27/0.97 (6) | 97.01/- | 96.26/- (14) | 97.76/- (15) | 88.18/0.82 | 88.63/0.83 (19) | 84.55/0.80 | 86.48/0.82 (18) | 90.43/0.86 (17) |
| 9 | 92.31/0.85 | 93.26/0.87 (14) | 93.84/- | 94.61/- (5) | 94.62/- (15) | 81.53/0.72 | 82.05/0.73 (20) | 82.33/0.76 | 82.36/0.77 (18) | 87.21/0.83 (14) |
| Avg. | 86.32/0.73 | 87.65/0.75 (13.2) | 80.56/- | 83.61/- (8.1) | 79.19/- (15) | 80.37/0.71 | 81.52/0.72 (17.4) | 76.03/0.68 | 77.18/0.70 (17.7) | 77.82/0.71 (15.2) |
| Std. | 8.96/0.18 | 8.42/0.17 (7.1) | 14.85/- | 11.35/- (4) | 15.85/- (-) | 9.78/0.15 | 9.21/0.14 (2.2) | 11.11/0.15 | 10.86/0.15 (2.5) | 13.52/0.17 (2.3) |
| Avg.* | | 87.24/0.75 (8.9) | | | | | 81.09/0.72 (13.7) | | 76.62/0.69 (14.2) | |
| Std.* | | 8.40/0.17 (6) | | | | | 9.23/0.14 (3.9) | | 10.95/0.15 (4.3) | |

* Taking the minimum number of channels while allowing a maximum accuracy degradation of 1%. See Appendix for the subject-specific values.

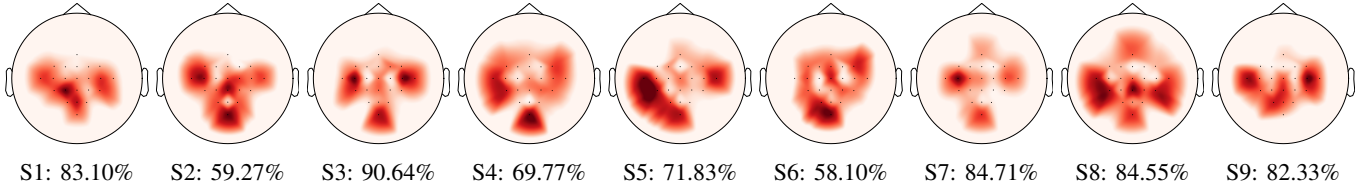


Fig. 4: Heatmaps of $\|w_S\|_2(i_{ch})$ on the IV-2a dataset averaged over 25 repetitions with 4-class full-channel accuracy. Darker red color represents higher values, meaning that the networks have learned stronger spatial weights.

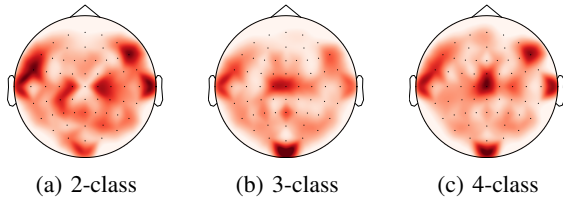


Fig. 5: Heatmaps of $\|w_S\|_2(i_{ch})$ on the MM/MI dataset averaged over 5-fold CV and 5 repetitions. Darker color indicates regions corresponding to stronger learned spatial weights.

subjects for 2-, 3-, and 4-class tasks are S8, S3, and S3, reaching up to 98.27%, 92.18%, and 90.97% with 6, 18, and 18 electrodes, respectively. Compared to the related works on this dataset, our subject-specific models achieve 4.04% and 8.46% better accuracy than [22] and [45] for the 2-class task, respectively, and 0.64% less accuracy than [46] for the 4-class task. The number of selected channels corresponding to the highest accuracy is vastly dependent on the subject, meaning that the trade-off between accuracy and resource usage has to be specifically assessed. An example is reported at the bottom of Table III, where we select the minimum number of channels for each subject while accepting an accuracy degradation of 1% at most. The average number of channels is further reduced while maintaining similar accuracy values.

The results on the MM/MI dataset confirm that the automatic method outperforms the manual methods. In general,

the simpler the task (i.e., 2-class), the less drop in accuracy. More precisely, we achieve almost the same accuracy as the baseline (82.79% and 74.92%) down to 10 and 20 channels (82.51% and 74.21%) for the 2- and 3-class classification, respectively. For the 4-class task, the accuracy drop is more significant, i.e., 1.69%, when reducing the number of channels to 18. Table IV reports the comparison with the related works. The full-channel model by [23] achieves 0.47% better accuracy than ours, at the cost of two orders of magnitude more memory requirement and $22\times$ more complexity. Whereas our channel selection method yields less accuracy drop (-0.15%) than [23] (-0.92%) using 14 EEG channels. The authors did not further reduce the number of channels. Compared to [44], [21], our method consistently achieves better accuracy at lower resource requirements. More specifically, a 14-channel configuration achieves 5.98% better accuracy with $38.5\times$ fewer parameters, $19.1\times$ smaller feature map size, and $16.9\times$ less computation than [44]. Compared to the method based on Granger causality proposed in [57], our solution is overall comparable, with slightly better accuracy when fewer channels are selected. With our method based on the spatial filters, we can decrease the number of EEG channels down to 10, i.e., by a factor of $6.4\times$, and still achieve comparable accuracy to the SoA with full-channel configuration, proving the effectiveness of our methods in extracting relevant features for the underlying task. Compared to the baseline MI-BMInet with 64 channels, using only 10 channels brings the advantage of $1.3\times$ fewer

parameters, $3.1\times$ less memory requirement, and $1.4\times$ less complexity in terms of MACCs, while retaining a similar classification accuracy of 82.51%.

We inspect the spatial filters of the trained models to gain insights into the brain activations. The average ℓ_2 -norm values of the spatial filters’ weights are depicted in Fig. 4 and Fig. 5. Each subject of the IV-2a dataset presents a different distribution over the scalp. Overall, the higher values are near the electrodes C3, C4 over the sensorimotor cortex and from the Cz to POz over the temporal lobe, indicating that the networks have learned stronger spatial weights for these regions. The analysis on the MM/MI dataset provides subject-independent, global information on the relevant brain regions. When considering the left- and right-hand tasks, the regions under the C3 and C4 have higher values. The addition of the ‘rest’ class introduces stronger learned weights around Iz over the occipital lobe, related to the visual cortex. The ‘feet’ class induces activations around Cz over the sensorimotor cortex. These findings are confirmed in the literature [10], [58]. We additionally observe activations near the electrodes F7 and F8. This is likely due to the presentation of the visual cues. We discuss possible lines of investigation in Sec. V.

C. Embedded Implementation

TABLE IV: Comparison of accuracy and resource requirements with channel selection on the MM/MI dataset. The estimated resources are calculated for the 4-class task when available, otherwise for the 2-class task. The proposed solutions are highlighted in bold.

| | # ch | Tot. # params | Max. # cons. f. | Tot. # MACC | Accuracy | | |
|-----------------------------|-----------|------------------|--------------------|----------------|--------------|--------------|--------------|
| | | | | | 2- | 3- | 4-class |
| S.ConvNet’18 [44] | 64 | 203 k | 1,260 k | 86.12 M | 80.38 | 69.82 | 58.58 |
| CNN’20 [23] | 64 | 235 k | 122.88 k | 33.61 M | 83.26 | - | - |
| EEGNet’20 [21] [§] | 64 | 3.17 k | 276.48 k | 48.17 M | 82.29 | 74.46 | 64.85 |
| MI-BMInet | 64 | 4.23 k | 38.40 k | 1.51 M | 82.79 | 74.92 | 65.62 |
| EEGNet’20 [21] [§] | 38 | 2.76 k | 164.16 k | 24.81 M | 81.86 | 74.12 | 64.65 |
| MI-BMInet | 38 | 3.81 k | 25.92 k | 1.31 M | 82.76 | 74.93 | 64.91 |
| CNN’20 [23] | 32 | 232 k | 61.44 k | 15.82 M | 82.90 | - | - |
| MI-BMInet | 32 | 3.49 k | 24.11 k | 1.26 M | 82.82 | 74.42 | 64.38 |
| EEGNet’20 [21] [§] | 19 | 2.35 k | 82.08 k | 11.02 M | 81.95 | 72.41 | 62.55 |
| MI-BMInet | 19 | 3.51 k | 16.8 k | 1.16 M | 82.78 | 74.02 | 63.69 |
| S.ConvNet’18 [44] | 16 | 126 k | 314.88 k | 21.6 M | 78.03 | - | - |
| MI-BMInet | 16 | 3.23 k | 15.36 k | 1.14 M | 82.63 | 73.47 | 63.47 |
| S.ConvNet’18 [44] | 14 | 123 k | 275.52 k | 18.92 M | 76.66 | - | - |
| CNN’20 [23] | 14 | 231 k | 26.88 k | 6.68 M | 82.34 | - | - |
| GCCS’21 [57] | 14 | - | - | - | 83.63 | - | - |
| MI-BMInet | 14 | 3.20 k | 14.40 k | 1.12 M | 82.64 | 72.89 | 63.30 |
| MI-BMInet | 10 | 3.14 k | 12.48 k | 1.09 M | 82.51 | 71.55 | 61.94 |
| S.ConvNet’18 [44] | 9 | 115 k | 177.12 k | 12.20 M | 75.85 | - | - |
| GCCS’21 [57] | 9 | - | - | - | 81.26 | - | - |
| MI-BMInet | 9 | 3.12 k | 12.00 k | 1.08 M | 82.06 | 71.24 | 61.44 |
| EEGNet’20 [21] [§] | 8 | 2.28 k | 34.56 k | 4.30 M | 78.07 | 68.99 | 58.55 |
| MI-BMInet | 8 | 3.33 k | 11.52 k | 1.08 M | 81.60 | 70.28 | 60.71 |
| S.ConvNet’18 [44] | 3 | 106 k | 59.04 k | 4.13 M | 73.20 | - | - |
| MI-BMInet | 3 | 3.03 k | 9.12 k | 1.04 M | 77.42 | 61.66 | 50.12 |

[§] Based on [20]. The reported accuracy is reproduced by averaging over five training/validation repetitions.

We use the PyTorch-based Quantlab framework [24] to quantize the models before the embedded deployment. As described in Sec. III-C, we perform quantization-aware training with STE and RPR algorithms. For the IV-2a dataset, $t_a=450$, $t_w=550$, and $t_{end}=650$ yield the best results. We use the cross-entropy loss and the Adam optimizer with a fixed learning rate of 0.001 and $\text{eps}=1e-7$. For the MM/MI dataset, we have $t_a=60$, $t_w=160$, and $t_{end}=260$. For the 3- and 4-class tasks, a fixed learning rate of 0.001 and $\text{eps}=1e-9$ yield the best results. Whereas for the 2-class task, the same learning rate scheduler as for the full-precision models is used with $\text{eps}=1e-9$.

The experimental results show that the quantized accuracy values are similar to the full-precision ones, with a maximum accuracy loss of 0.4%. More precisely, the values for 2-, 3-, 4-class tasks are 86.52%, 80.05%, 75.63% (IV-2a), and 82.61%, 75.12%, 65.31% (MM/MI), respectively. The quantization of both weights and activations allows $4\times$ reduction of the total memory footprint. More specifically, the memory requirement is reduced from around 186 kB and 171 kB when using 32-bit representation down to roughly 47 kB and 43 kB with 8-bit quantization for the IV-2a and MM/MI datasets, respectively. Recall that the fast L1 memory of Mr. Wolf is only 64 kB [19]. Hence, with a memory footprint of less than 50 kB, we effectively eliminate the data transfer between the L1 and L2 memory during the computation of a single layer, reducing double-buffering overheads while maintaining similar classification accuracy. As illustrated in Fig. 6, most related works do not fit in the fast memory of Mr. Wolf and Vega, especially without quantization. The memory requirement of the quantized MI-BMInet is up to four orders of magnitude lower, and it is within the tightest memory constraint (64 kB). It also requires the least amount of MACCs.

We measure the power consumption and the inference runtime of the deployed models using the Keysight N6705B power analyzer (61.44 μs sampling interval), including all op-

TABLE V: Networks deployment and measurement results. All Mr. Wolf cores run at 50 MHz with 0.8 V power supply as in [13]. The SoC core of Vega runs at 50 MHz and the cluster cores at 160 MHz as in [29]. The power supply is 0.65 V.

| Dataset | BCI Comp. | | | Physionet | | |
|---------------------------------|-----------|-------|----------------|-----------|--------------|-----------------|
| | 4 | 2 | 2 | 4 | 2 | 2 |
| Num. classes | 4 | 2 | 2 | 4 | 2 | 2 |
| Num. channels | 22 | 22 | 6 [†] | 64 | 64 | 10 [‡] |
| (Q) Accuracy (%) | 75.63 | 86.52 | 97.76 | 65.31 | 82.61 | 82.51 |
| Est. Memory (kB) | 46.58 | 45.88 | 33.37 | 42.63 | 42.40 | 15.62 |
| Est. #MACCs (M) | 2.21 | 2.21 | 1.82 | 1.51 | 1.51 | 1.09 |
| Mr. Wolf | | | | | | |
| Time/infer. (ms) | 11.37 | 11.30 | 10.57 | 6.21 | 6.21 | 5.53 |
| Avg. power (mW) | 10.07 | 10.24 | 9.70 | 9.92 | 10.00 | 9.06 |
| Energy/infer. (μJ) | 114.5 | 115.7 | 102.5 | 61.60 | 62.10 | 50.10 |
| Throughput (MMACCs/s) | 194.3 | 195.5 | 172.6 | 242.5 | 242.4 | 197.2 |
| En. Eff. (GMACCs/s/W) | 19.30 | 19.09 | 17.80 | 24.44 | 24.24 | 21.77 |
| Vega | | | | | | |
| Time/infer. (ms) | 5.10 | 4.85 | 4.73 | 3.19 | 3.13 | 2.95 |
| Avg. power (mW) | 11.87 | 12.07 | 11.52 | 11.40 | 11.28 | 10.17 |
| Energy/infer. (μJ) | 60.5 | 58.5 | 54.5 | 36.4 | 35.3 | 30.0 |
| Throughput (MMACCs/s) | 433.3 | 455.7 | 384.8 | 473.4 | 482.4 | 369.5 |
| En. Eff. (GMACCs/s/W) | 36.50 | 37.75 | 33.40 | 41.52 | 42.77 | 36.33 |

[†] Subject 8. Selected channels: CP3, P1, POz, CP4, C6, FC4.

[‡] Fold 1. Sel. channels: AF8, F8, T8, C3, Cz, C2, CP2, CP5, F6, T9.

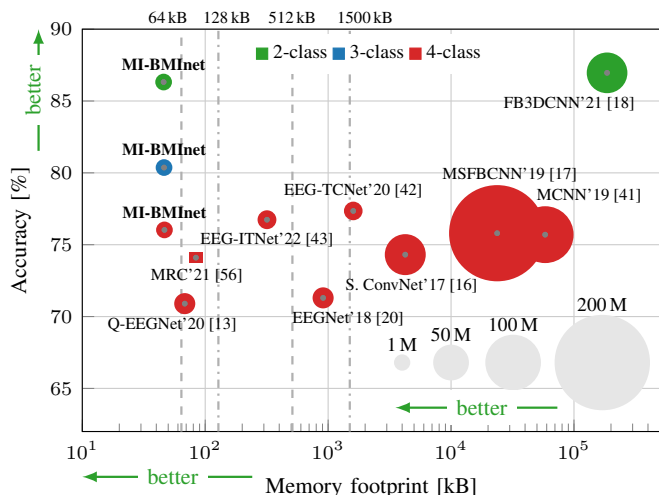


Fig. 6: Accuracy vs. memory footprint on the IV-2a dataset. The number of MACCs is represented as the size of the circles, while the square indicates that it is variable. The memory footprint includes both parameters and features (see Table II). The precision is assumed to be 32 bits if no quantization is proposed. The dashed and dash-dotted lines mark the L1 and L2 memory of Mr. Wolf and Vega, respectively.

eration domains of the selected microprocessors and the cluster startup time. We set the clock frequency of the cores to the same values as in [13] and [29] for a fair comparison. Table V shows the results. The measured inference runtime on Mr. Wolf is around 11.4ms for the IV-2a dataset in full-channel configuration and 6.2 ms for the MM/MI dataset. The average power consumption is roughly 10mW, yielding an energy consumption per inference of 115 μ J and 62 μ J, respectively. The execution time on Vega is more than twice faster and consumes down to 36 μ J. Fig. 7 depicts the comparison with the related works. Our implementation is orders of magnitude faster and less energy-hungry. Compared to the most energy-efficient model with the same MCU configurations [29], our solution is 3.3 \times faster and more energy-efficient and achieves higher classification accuracy. The channel reduction further reduces the runtime and the energy consumption. Considering the best performing subject (S8, 98.27% accuracy) of the IV-2a dataset on the 2-class task, the number of EEG channels can be decreased to 6 while keeping similar classification accuracy (97.76%). It yields an energy reduction of approximately 10% compared to the usage of all 22 channels. We can draw the same conclusion for the subject-independent MM/MI dataset. We successfully decrease the number of channels by a factor of 6.4 \times (from 64 to 10) without significant accuracy loss for the 2-class task. It translates into a runtime speedup of 1.1 \times and an energy reduction of 15%, i.e., down to 30 μ J. Overall, the highest achieved throughput is 482.4 MMACCs/s with an energy efficiency of 42.77 GMACCs/s/W.

V. DISCUSSION

The proposed CNN achieves similar accuracy as the most recent related works [42], [18], [43], [23], while being significantly more hardware-friendly. Note that our accuracy

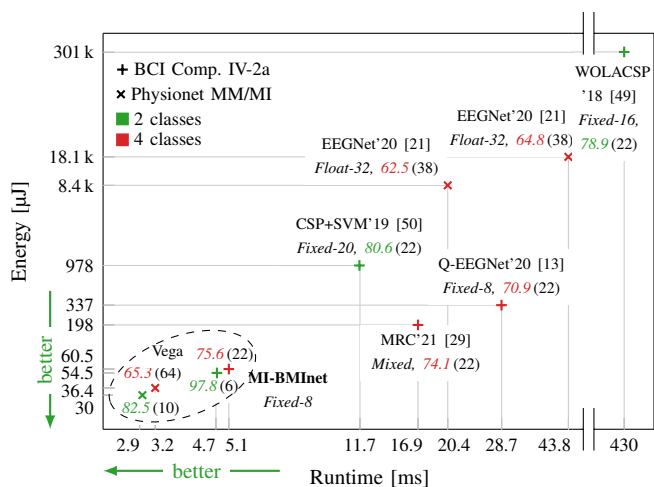


Fig. 7: Energy consumption vs. runtime. The numerical precision and the accuracy (%) of the embedded implementation are reported in *italic*. The number of EEG channels is in brackets.

values are averaged over multiple runs to account for the variability caused by the non-deterministic behavior of the training algorithms for a better statistical significance. The standard deviation among the training repetitions on the IV-2a dataset is at least 1.3% [13]. Hence, our achieved accuracy is comparable to the related works. The additional technique of subject-specific hyperparameters tunings proposed in [42] has improved the accuracy to almost 84%. This further strengthens the evidence that subject-specific network architectures (e.g., variable kernel sizes, different number of filters) lead to significant accuracy gains. This technique can be easily adapted to the proposed CNN, and similar improvements can be expected.

Notwithstanding, MI-BMInet has roughly 10 \times less memory footprint and 3 \times fewer computations than [42], enabling its deployment on ultra-low-power MCUs with real-time inference. The extraction of spatial information before the temporal features substantially reduces resource usage. It is a universal and effective technique that all related networks in Table II can adopt to lower their resource demands, especially the recent ones with multiple parallel convolutional blocks [17], [41], [43]. Future directions can investigate subject-specific neural architecture search while being aware of the memory and computation burdens related to the order of the operations. EEG-ITNet requires also relatively small resource usage thanks to the downsampling of the input EEG signals [43]. It is also an effective way to reduce the model size as demonstrated in [21], and it can be considered as a preprocessing stage in addition to our methods.

The proposed channel reduction algorithm further reduces the resource requirements while retaining similar accuracy. It additionally lowers the power consumption of the data acquisition stage. Considering the same setup as in [12], i.e., 0.965 mW/channel, 1.26 mW for the digital section excluding the processing, and a 65 mAh battery, the reduction from 64 to 10 channels yields an increased battery life from 3.8 to 22 hours with the negligible consumption of 0.03 mW using

Vega or 0.05 mW using Mr. Wolf, assuming a continuous classification every second.

The inspection of the spatial filters gives insights into the relevant brain regions for MI tasks. Especially interesting are the activations around F7 and F8 electrodes. They cover the inferior frontal gyrus near the Sylvian fissure between the frontal and temporal lobe, where the insular cortex is located [59], [60]. This area is considered relevant in attentional elaborations and working memory processing related to external stimuli [61], [62]. Being part of the dorsal frontoparietal network, it has a top-down control function over motor and sensory areas with the basic cognitive selection of sensory information and response [63]. Moreover, a study suggests that it plays a role in motor planning and imagery [64]. A similar line of research on the insular cortex, saccade system, and supplementary motor areas further confirms the involvement of this area in motor control, attentional fixation, and responses to switching stimuli [65], [66]. Another study suggests that the activities in this area are due to electromyographic and electrooculographic artifacts [44]. Depending on the acquisition setup, this is also a valid hypothesis since the electrodes F7 and F8 are prone to collect muscular and ocular artifacts [67]. An acquisition procedure that eliminates the dependency on the visual cue is helpful in future research to investigate the fundamental nature of this activation. A possible solution is to design an experimental paradigm combined with electromyograms [68].

Another future research direction is the detection of movement intention. For a real-world IoM scenario, no visual cue is presented to the subject marking the MI's start. Hence, algorithms that can autonomously detect the onset of the MI intention are necessary for an online BMI that is asynchronously self-paced.

VI. CONCLUSION

This paper proposes an energy-efficient embedded solution for MI-BMIs. We design a tiny CNN that achieves similar SoA accuracy but is orders of magnitude less resource-demanding. We further propose an automatic channel reduction method based on spatial filters and extract the most relevant EEG channels to effectively reduce the memory requirements, the computational complexity, and the power consumption. We finally deploy the proposed models on ultra-low-power MCUs and experimentally measure the runtime and the energy consumption. The final solution consumes down to 30 μ J and takes only 2.95 ms per inference with an accuracy of 82.51% on the 2-class MI task using only 10 instead of 64 EEG channels, yielding an operation of up to 22 hours. By combining a model design that is aware of the resource usage, the channel reduction and the quantization techniques, and an embedded implementation that optimally exploits the underlying hardware architecture, we satisfy the three-way trade-off among accuracy performance, resource usage, and power consumption, setting the new SoA for next-generation wearable BMIs with smart edge computing.

REFERENCES

[1] M. Xiong, R. Hotter, D. Nadin *et al.*, "A low-cost, semi-autonomous wheelchair controlled by motor imagery and jaw muscle activation," in

Proc. IEEE International Conference on Systems, Man and Cybernetics (SMC), 2019, pp. 2180–2185.

[2] M. Vilela and L. R. Hochberg, "Chapter 8 - applications of brain-computer interfaces to the control of robotic and prosthetic arms," in *Brain-Computer Interfaces*, ser. Handbook of Clinical Neurology, N. F. Ramsey and J. del R. Millán, Eds. Elsevier, 2020, vol. 168, pp. 87–99.

[3] U. Chaudhary, N. Birbaumer, and A. Ramos-Murguialday, "Brain-computer interfaces for communication and rehabilitation," *Nature Reviews Neurology*, vol. 12, pp. 513–525, 08 2016.

[4] A. Casson, "Wearable EEG and beyond," *Biomedical Engineering Letters*, vol. 9, pp. 53–71, 01 2019.

[5] P. Aricò, N. Sciaraffa, and F. Babiloni, "Brain-computer interfaces: Toward a daily life employment," *Brain Sciences*, vol. 10, no. 3, 03 2020.

[6] L. Shao, L. Zhang, A. N. Belkacem *et al.*, "EEG-controlled wall-crawling cleaning robot using SSVEP-based brain-computer interface," *Journal of Healthcare Engineering*, vol. 2020, pp. 1–11, 01 2020.

[7] N. Kobayashi and K. Ishizuka, "LSTM-based classification of multiflicker-SSVEP in single channel dry-EEG for low-power/high-accuracy quadcopter-BMI system," in *Proc. IEEE International Conference on Systems, Man and Cybernetics (SMC)*, 2019, pp. 2160–2165.

[8] A. N. Belkacem, N. Jamil, J. A. Palmer, S. Ouhbi, and C. Chen, "Brain computer interfaces for improving the quality of life of older adults and elderly patients," *Frontiers in Neuroscience*, vol. 14, p. 692, 2020.

[9] D. Freer and G.-Z. Yang, "Data augmentation for self-paced motor imagery classification with C-LSTM," *Journal of Neural Engineering*, vol. 17, no. 1, p. 016041, 01 2020.

[10] G. Pfurtscheller and F. Lopes da Silva, "Event-related EEG/MEG synchronization and desynchronization: basic principles," *Clinical Neurophysiology*, vol. 110, no. 11, pp. 1842–1857, 11 1999.

[11] J. Zhuang, K. Geng, and G. Yin, "Ensemble learning based brain-computer interface system for ground vehicle control," *IEEE Transactions on Systems, Man, and Cybernetics: Systems*, vol. 51, no. 9, pp. 5392–5404, 2021.

[12] V. Kartsch, G. Tagliavini, M. Guermandi *et al.*, "BioWolf: A sub-10-mW 8-channel advanced brain-computer interface platform with a nine-core processor and BLE connectivity," *IEEE Transactions on Biomedical Circuits and Systems*, vol. 13, no. 5, pp. 893–906, 2019.

[13] T. Schneider, X. Wang, M. Hersche, L. Cavigelli, and L. Benini, "Q-EEGNet: an energy-efficient 8-bit quantized parallel EEGNet implementation for edge motor-imagery brain-machine interfaces," in *Proc. IEEE International Conference on Smart Computing (SMARTCOMP)*, 2020, pp. 284–289.

[14] C. Beach, E. Balaban, and A. J. Casson, "Chapter 14 - Edge algorithms for wearables: an overview of a truly multi-disciplinary problem," in *Wearable Sensors*, 2nd ed., E. Sazonov, Ed. Oxford: Academic Press, 2021, pp. 379–414.

[15] E. Tunstel, M. J. Cobo, E. Herrera-Viedma *et al.*, "Systems science and engineering research in the context of systems, man, and cybernetics: Recollection, trends, and future directions," *IEEE Transactions on Systems, Man, and Cybernetics: Systems*, vol. 51, no. 1, pp. 5–21, 2021.

[16] R. T. Schirmer, J. T. Springenberg, L. D. J. Fiederer *et al.*, "Deep learning with convolutional neural networks for EEG decoding and visualization," *Human Brain Mapping*, vol. 38, no. 11, pp. 5391–5420, 2017.

[17] H. Wu, Y. Niu, F. Li *et al.*, "A parallel multiscale filter bank convolutional neural networks for motor imagery EEG classification," *Frontiers in Neuroscience*, vol. 13, 11 2019.

[18] J. S. Bang, M. H. Lee, S. Fazli, C. Guan, and S. W. Lee, "Spatio-spectral feature representation for motor imagery classification using convolutional neural networks," *IEEE Transactions on Neural Networks and Learning Systems*, pp. 1–12, 2021.

[19] A. Pullini, D. Rossi, I. Loi, G. Tagliavini, and L. Benini, "Mr.Wolf: An energy-precision scalable parallel ultra low power SoC for IoT edge processing," *IEEE Journal of Solid-State Circuits*, vol. 54, no. 7, pp. 1970–1981, 2019.

[20] V. J. Lawhern, A. J. Solon, N. R. Waytowich *et al.*, "EEGNet: a compact convolutional neural network for EEG-based brain-computer interfaces," *Journal of Neural Engineering*, vol. 15, no. 5, p. 056013, 2018.

[21] X. Wang, M. Hersche, B. Tömeke *et al.*, "An accurate EEGNet-based motor-imagery brain-computer interface for low-power edge computing," in *2020 IEEE International Symposium on Medical Measurements and Applications (MeMeA)*, 2020, pp. 1–6.

[22] A. K. Das and S. Suresh, "An effect-size based channel selection algorithm for mental task classification in brain computer interface," in *2015 IEEE International Conference on Systems, Man, and Cybernetics*, 2015, pp. 3140–3145.

- [23] M. Tokovarov, "Convolutional neural networks with reusable full-dimension-long layers for feature selection and classification of motor imagery in EEG signals," in *Artificial Neural Networks and Machine Learning - ICANN 2020*. Springer International Publishing, 2020, pp. 79–91.
- [24] M. Spallanzani, L. Cavigelli, G. Leonardi, M. Bertogna, and L. Benini, "Additive noise annealing and approximation properties of quantized neural networks," *arXiv:1905.10452*, 05 2019.
- [25] L. Cavigelli and L. Benini, "RPR: Random partition relaxation for training; binary and ternary weight neural networks," *arXiv:2001.01091*, 2020.
- [26] D. Rossi, F. Conti, M. Eggiman *et al.*, "A 1.3TOPS/W @ 32GOPS fully integrated 10-core SoC for IoT end-nodes with 1.7uW cognitive wake-up from MRAM-based state-retentive sleep mode," in *2021 IEEE International Solid-State Circuits Conference (ISSCC)*, vol. 64, 2021, pp. 60–62.
- [27] X. Wang, M. Magno, L. Cavigelli, and L. Benini, "Fann-on-mcu: An open-source toolkit for energy-efficient neural network inference at the edge of the internet of things," *IEEE Internet of Things Journal*, vol. 7, no. 5, pp. 4403–4417, 2020.
- [28] A. Garofalo, M. Rusci, F. Conti, D. Rossi, and L. Benini, "PULP-NN: accelerating quantized neural networks on parallel ultra-low-power RISC-V processors," *Phil. Trans. R. Soc. A.*, 12 2019.
- [29] X. Wang, L. Cavigelli, T. Schneider, and L. Benini, "Sub-100 μ w multispectral riemannian classification for eeg-based brain-machine interfaces," *IEEE Transactions on Biomedical Circuits and Systems*, vol. 15, no. 6, pp. 1149–1160, 2021.
- [30] C. Brunner, R. Leeb, G. R. Müller-Putz, A. Schlögl, and G. Pfurtscheller, "BCI competition 2008 - Graz data set A," doi: 10.1007/BF00994018.
- [31] M. Tangermann, K.-R. Müller, A. Aertsen *et al.*, "Review of the BCI competition IV," *Frontiers in Neuroscience*, vol. 6, p. 55, 2012.
- [32] G. Schalk, D. McFarland, T. Hinterberger, N. Birbaumer, and J. Wolpaw, "BCI2000: a general-purpose brain-computer interface BCI system," *IEEE Transactions on Biomedical Engineering*, vol. 51, no. 6, pp. 1034–1043, 2004.
- [33] A. L. Goldberger, L. A. N. Amaral, L. Glass *et al.*, "PhysioBank, PhysioToolkit, and PhysioNet: components of a new research resource for complex physiologic signals," *circulation*, vol. 101, no. 23, pp. e215–e220, 2000.
- [34] K. K. Ang, Z. Y. Chin, C. Wang, C. Guan, and H. Zhang, "Filter bank common spatial pattern algorithm on BCI competition IV datasets 2a and 2b," *Frontiers in Neuroscience*, vol. 6, p. 39, 2012.
- [35] B. Chen, Y. Li, J. Dong, N. Lu, and J. Qin, "Common spatial patterns based on the quantized minimum error entropy criterion," *IEEE Transactions on Systems, Man, and Cybernetics: Systems*, vol. 50, no. 11, pp. 4557–4568, 2020.
- [36] F. Yger, M. Berar, and F. Lotte, "Riemannian approaches in brain-computer interfaces: A review," *IEEE Transactions on Neural Systems and Rehabilitation Engineering*, vol. 25, no. 10, pp. 1753–1762, 10 2017.
- [37] A. Jiang, J. Shang, X. Liu *et al.*, "Efficient CSP algorithm with spatio-temporal filtering for motor imagery classification," *IEEE Transactions on Neural Systems and Rehabilitation Engineering*, vol. 28, no. 4, pp. 1006–1016, 2020.
- [38] M. Hersche, T. Rellstab, P. D. Schiavone *et al.*, "Fast and Accurate Multiclass Inference for MI-BCIs Using Large Multiscale Temporal and Spectral Features," in *Proc. 26th European Signal Processing Conference (EUSIPCO)*. IEEE, 9 2018, pp. 1690–1694.
- [39] J. Wang, Z. Feng, X. Ren *et al.*, "Feature subset and time segment selection for the classification of eeg data based motor imagery," *Biomedical Signal Processing and Control*, vol. 61, p. 102026, 2020.
- [40] R. Das, P. S. Lopez, M. Ahmed Khan, H. K. Iversen, and S. Puthusserypady, "FBCSP and adaptive boosting for multiclass motor imagery BCI data classification: A machine learning approach," in *Proc. IEEE International Conference on Systems, Man, and Cybernetics (SMC)*, 2020, pp. 1275–1279.
- [41] S. U. Amin, M. Alsulaiman, G. Muhammad, M. A. Mekhtiche, and M. Shamim Hossain, "Deep learning for EEG motor imagery classification based on multi-layer CNNs feature fusion," *Future Generation Computer Systems*, vol. 101, pp. 542–554, 2019.
- [42] T. M. Ingolfsson, M. Hersche, X. Wang *et al.*, "EEG-TCNet: An accurate temporal convolutional network for embedded motor-imagery brain-machine interfaces," in *Proc. IEEE International Conference on Systems, Man, and Cybernetics (SMC)*, 2020, pp. 2958–2965.
- [43] A. Salami, J. Andreu-Perez, and H. Gillmeister, "EEG-ITNet: An explainable inception temporal convolutional network for motor imagery classification," *IEEE Access*, vol. 10, pp. 36 672–36 685, 2022.
- [44] H. Dose, J. S. Møller, H. K. Iversen, and S. Puthusserypady, "An end-to-end deep learning approach to MI-EEG signal classification for BCIs," *Expert Systems with Applications*, vol. 114, pp. 532–542, 2018.
- [45] P. Gaur, R. B. Pachori, H. Wang, and G. Prasad, "An automatic subject specific intrinsic mode function selection for enhancing two-class eeg-based motor imagery-brain computer interface," *IEEE Sensors Journal*, vol. 19, no. 16, pp. 6938–6947, 2019.
- [46] S. Chen, Y. Sun, H. Wang, and Z. Pang, "Channel selection based similarity measurement for motor imagery classification," in *Proc. IEEE International Conference on Bioinformatics and Biomedicine (BIBM)*, 2020, pp. 542–548.
- [47] TinyML Foundation, "tinyML[®]," <https://www.tinyml.org/>, 2021, accessed: 2021-05-27.
- [48] R. David, J. Duke, A. Jain *et al.*, "TensorFlow Lite Micro: Embedded machine learning on TinyML systems," *arXiv:2010.08678*, 2021.
- [49] K. Belwafi, O. Romain, S. Gannouni *et al.*, "An embedded implementation based on adaptive filter bank for brain-computer interface systems," *Journal of Neuroscience Methods*, vol. 305, pp. 1–16, 2018.
- [50] A. Malekmohammadi, H. Mohammadzade, A. Chamanzar, M. Shabany, and B. Ghoghj, "An efficient hardware implementation for a motor imagery brain computer interface system," *Scientia Iranica*, vol. 26, no. Special Issue on: Socio-Cognitive Engineering, pp. 72–94, 2019.
- [51] L. Lai, N. Suda, and V. Chandra, "Not all ops are created equal!" *ArXiv*, vol. abs/1801.04326, 2018.
- [52] N. M. LLC, "Versus: a mobile EEG headset," <https://getversus.com/>, 2021, accessed: 2021-10-11.
- [53] G. Spinelli, A. Odouard, M.-C. Nierat *et al.*, "Validation of melo-mind™ signal quality: a proof of concept resting-state and ERPs study," *bioRxiv:2020.02.28.969808*, 2020.
- [54] B. Jacob, S. Kligys, B. Chen *et al.*, "Quantization and training of neural networks for efficient integer-arithmetic-only inference," in *Proc. IEEE CVPR*, 2018, pp. 2704–2713.
- [55] X. Wang, "DSP library for PULP," <https://github.com/pulp-platform/pulp-dsp>, 2019.
- [56] X. Wang, T. Schneider, M. Hersche, L. Cavigelli, and L. Benini, "Mixed-precision quantization and parallel implementation of multispectral riemannian classification for brain-machine interfaces," in *Proc. IEEE International Symposium on Circuits and Systems (ISCAS)*, 2021, pp. 1–5.
- [57] H. Varsehi and S. M. P. Firoozabadi, "An eeg channel selection method for motor imagery based brain-computer interface and neurofeedback using granger causality," *Neural Networks*, vol. 133, pp. 193–206, 2021.
- [58] M. Zhao, M. Marino, J. Samogin, S. P. Swinnen, and D. Mantini, "Hand, foot and lip representations in primary sensorimotor cortex: a high-density electroencephalography study," *Brain Connectivity*, vol. 9, pp. 2045–2322, 2019.
- [59] R. Homan, J. Herman, and P. Purdy, "Cerebral location of international 10-20 system electrode placement," *Electroencephalography and Clinical Neurophysiology*, vol. 66, no. 4, pp. 376–82, 1987.
- [60] V. L. Towle, J. Bolaños, D. Suarez *et al.*, "The spatial location of EEG electrodes: locating the best-fitting sphere relative to cortical anatomy," *Electroencephalography and Clinical Neurophysiology*, vol. 86, no. 1, pp. 1–6, 1993.
- [61] M. Tops and M. Boksem, "A potential role of the inferior frontal gyrus and anterior insula in cognitive control, brain rhythms, and event-related potentials," *Frontiers in Psychology*, vol. 2, p. 330, 2011.
- [62] M. Corbetta, G. Patel, and G. Shulman, "The reorienting system of the human brain: from environment to theory of mind," *Neuron*, vol. 58, no. 3, pp. 306–24, 2008.
- [63] M. Corbetta and G. Shulman, "Control of goal-directed and stimulus-driven attention in the brain," *Nature Reviews Neuroscience*, vol. 3, no. 3, pp. 201–15, 2008.
- [64] R. Ptak, A. Schnider, and J. Fellrath, "The dorsal frontoparietal network: A core system for emulated action," *Trends in Cognitive Sciences*, vol. 21, no. 8, pp. 589–599, 2017.
- [65] T. J. Anderson, I. H. Jenkins, D. J. Brooks *et al.*, "Cortical control of saccades and fixation in man. A PET study," *Brain*, vol. 117, no. 5, pp. 1073–1084, 10 1994.
- [66] P. Nachev, C. Kennard, and M. Husain, "Functional role of the supplementary and pre-supplementary motor areas," *Nature Reviews Neuroscience*, vol. 9, no. 11, pp. 856–869, 2008.
- [67] M. Sazgar and M. G. Young, *EEG Artifacts*. Springer International Publishing, 2019, pp. 149–162.
- [68] R. Xu, N. Jiang, N. Mrachacz-Kersting *et al.*, "A closed-loop brain-computer interface triggering an active ankle-foot orthosis for inducing cortical neural plasticity," *IEEE Transactions on Biomedical Engineering*, vol. 61, no. 7, pp. 2092–2101, 2014.



Xiaying Wang received her B.Sc. and M.Sc. degrees in biomedical engineering from Politecnico di Milano, Italy, and ETH Zürich, Switzerland, in 2016 and 2018, respectively. She is currently pursuing a Ph.D. degree at the Integrated Systems Laboratory at ETH Zürich. Her research interests include biosignal processing, brain-machine interface, low power embedded systems, energy-efficient smart sensors, and machine learning on microcontrollers. She received the excellent paper award at the IEEE Healthcom conference in 2018 and won the Ph.D. Fellowship

funded by the Swiss Data Science Center in 2019.



Michael Hersche received his M.Sc. degree from the Swiss Federal Institute of Technology Zurich (ETHZ), Switzerland, where he is currently pursuing a Ph.D. degree. Since 2019, he has been a Research Assistant with ETHZ in the group of Prof. L. Benini at the Integrated Systems Laboratory. His research interests include digital signal processing, artificial intelligence, and communications with focus on hyperdimensional computing. He received the 2020 IBM Ph.D. Fellowship Award.



Michele Magno received his master's and Ph.D. degrees in electronic engineering from the University of Bologna, Bologna, Italy, in 2004 and 2010, respectively. He is currently a Senior Researcher and lecturer with ETH Zürich, Switzerland. He has authored more than 150 papers in international journals and conferences, a few of them awarded as best papers. His current research interests include wireless sensor networks, wearable devices, energy harvesting, low power management techniques, and extension of the lifetime of batteries-operating devices.

devices.



Luca Benini is the Chair of Digital Circuits and Systems at ETH Zürich and a Full Professor at the University of Bologna. He has served as Chief Architect for the Platform2012 in STMicroelectronics, Grenoble. Dr. Benini's research interests are in energy-efficient systems and multi-core SoC design. He is also active in the area of energy-efficient smart sensors and sensor networks. He has published more than 1'000 papers in peer-reviewed international journals and conferences, four books, and several book chapters. He is a Fellow of the ACM and the

IEEE and a member of the Academia Europaea.

APPENDIX

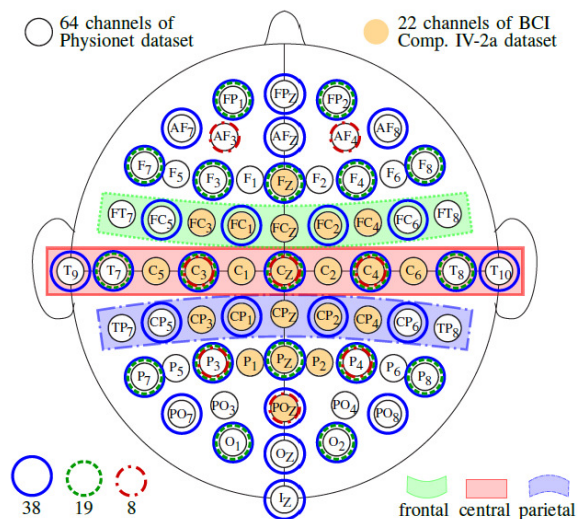


Fig. 8: Electrode configurations for manual channel selections.

TABLE VI: EEG electrodes configurations using headset-based channel selection over sensorimotor and neighboring areas. The regions correspond to the brain areas with color-shaded background illustrated in Fig. 8, as well as the electrodes, while N_{ch} is the number of selected channels.

| Region | N_{ch} | Electrodes |
|-------------|--|--|
| Central (C) | 2 | C3, C4 |
| | 3 | C3, CZ, C4 |
| | 5 | C5, C3, CZ, C4, C6 |
| | 7 | C5, C3, C1, CZ, C2, C4, C6 |
| | 9 | T7, C5, C3, C1, CZ, C2, C4, C6, T8 |
| 11 | T9, T7, C5, C3, C1, CZ, C2, C4, C6, T8, T10 | |
| C+Frontal | 4 | C3, C4, FC3, FC4 |
| | 6 | C3, CZ, C4, FC3, FCZ, FC4 |
| | 10 | C5, C3, CZ, C4, C6, FC5, FC3, FCZ, FC4, FC6 |
| | 14 | C5, C3, C1, CZ, C2, C4, C6, FC5, FC3, FC1, FCZ, FC2, FC4, FC6 |
| | 18 | T7, C5, C3, C1, CZ, C2, C4, C6, T8, FT7, FC5, FC3, FC1, FCZ, FC2, FC4, FC6, FT8 |
| 20 | T9, T7, C5, C3, C1, CZ, C2, C4, C6, T8, T10, FT7, FC5, FC3, FC1, FCZ, FC2, FC4, FC6, FT8 | |
| C+Parietal | 4 | C3, C4, CP3, CP4 |
| | 6 | C3, CZ, C4, CP3, CPZ, CP4 |
| | 10 | C5, C3, CZ, C4, C6, CP5, CP3, CPZ, CP4, CP6 |
| | 14 | C5, C3, C1, CZ, C2, C4, C6, CP5, CP3, CP1, CPZ, CP2, CP4, CP6 |
| | 18 | T7, C5, C3, C1, CZ, C2, C4, C6, T8, TP7, TP7, CP5, CP3, CP1, CPZ, CP2, CP4, CP6, TP8 |
| 20 | T9, T7, C5, C3, C1, CZ, C2, C4, C6, T8, T10, TP7, CP5, CP3, CP1, CPZ, CP2, CP4, CP6, TP8 | |

TABLE VII: Classification accuracy (%) / kappa score of MI-BMNet with all channels and with the minimum number of selected channels (in brackets) when allowing a maximum accuracy degradation of 1% on the IV-2a dataset.

| S. | 2-class | | 3-class | | 4-class | |
|------|------------|------------------|------------|-------------------|------------|-------------------|
| | all ch. | sel. ch. | all ch. | sel. ch. | all ch. | sel. ch. |
| 1 | 84.03/0.68 | 86.98/0.74 (4) | 89.43/0.84 | 91.03/0.87 (6) | 83.10/0.78 | 83.89/0.79 (14) |
| 2 | 71.15/0.42 | 72.03/0.44 (16) | 65.74/0.49 | 68.76/0.53 (16) | 59.27/0.46 | 59.52/0.46 (16) |
| 3 | 94.95/0.90 | 94.10/0.88 (4) | 91.67/0.88 | 91.65/0.88 (16) | 90.64/0.88 | 90.97/0.88 (18) |
| 4 | 74.38/0.49 | 76.07/0.52 (4) | 75.66/0.64 | 76.00/0.64 (14) | 69.77/0.60 | 70.63/0.61 (18) |
| 5 | 92.00/0.84 | 93.84/0.88 (4) | 79.17/0.70 | 79.54/0.69 (10) | 71.83/0.62 | 72.64/0.64 (10) |
| 6 | 79.48/0.59 | 81.11/0.62 (20) | 63.48/0.45 | 64.69/0.47 (16) | 58.10/0.44 | 59.42/0.46 (4) |
| 7 | 90.51/0.81 | 90.63/0.81 (14) | 88.49/0.83 | 88.57/0.83 (16) | 84.71/0.80 | 84.90/0.80 (16) |
| 8 | 98.06/0.96 | 97.76/0.96 (4) | 88.18/0.82 | 88.26/0.82 (10) | 84.55/0.80 | 85.93/0.81 (16) |
| 9 | 92.31/0.85 | 92.62/0.85 (10) | 81.53/0.72 | 81.33/0.72 (19) | 82.33/0.76 | 81.67/0.76 (16) |
| Avg. | 86.32/0.73 | 87.24/0.75 (8.9) | 80.37/0.71 | 81.09/0.72 (13.7) | 76.03/0.68 | 76.62/0.69 (14.2) |
| Std. | 8.96/0.18 | 8.40/0.17 (6) | 9.78/0.15 | 9.23/0.14 (3.9) | 11.11/0.15 | 10.95/0.15 (4.3) |